

# Estimating mass and momentum fluxes in a line of cumulonimbus using a single high-resolution Doppler radar

Robin J. Hogan\*, Anthony J. Illingworth and Kate Halladay

*Department of Meteorology, University of Reading, UK*

**ABSTRACT:** We present a method to derive the vertical-wind field at a scale of 1–2 km from a high-resolution Doppler radar, by performing vertical scans in the plane of the mean wind and tracking turbulent features on a scale of several hundred metres in the radial-velocity field between consecutive scans. The method is applied to a line of cumulonimbus clouds observed by the high-resolution Chilbolton radar in southern England. The storm was not a squall line, since it was propagating parallel rather than perpendicular to its length. A sequence of scans was taken over an hour-long period; from these scans we derive the  $u$  and  $w$  components of the wind. Updraughts of up to  $15 \text{ m s}^{-1}$  are found.

From these observations, the mass flux of a ‘typical’ storm cell was estimated: over the 50 min lifetime of the cell, the total mass of air transported from the boundary layer to the upper troposphere was found to be around 50 megatonnes. The profile of hour-averaged momentum flux against height was then calculated and compared to the vertical shear of the mean horizontal wind. It was found that above 4.5 km, the momentum flux was down-gradient, with an equivalent eddy diffusivity of around  $10^3 \text{ m}^2 \text{s}^{-1}$ . Below this height, however, the flux was counter-gradient, with an equivalent eddy diffusivity of around  $-10^3 \text{ m}^2 \text{s}^{-1}$ . We propose a mechanism to explain this behaviour, involving the prevalence of precipitation cooling and descent on the downshear side of convergence lines.

A synthesis of the major wind flows in the storm reveals that, despite superficial appearance, the storm did not fit the usual multi-cell paradigm, in which gust fronts play a key role in triggering new cells downwind. Rather, the convergence lines associated with the convection were more akin to warm frontal surfaces that remain tied to the base of each cell, new cells tending to form upwind of older cells. Copyright © 2008 Royal Meteorological Society

KEY WORDS back-building storm; Doppler radar; updraught; up-gradient momentum flux

Received 20 December 2007; Revised 25 May 2008; Accepted 9 June 2008

## 1. Introduction

It is known that momentum transport by convective storms can have a significant influence on the large-scale flow (Houze, 1973). However, when parametrizing this in numerical models, one difficulty is that the magnitude and even the sign of the transport is sensitive to the configuration of the convective-scale updraughts and downdraughts, which in turn depend on the ambient wind-shear profile (Moncrieff, 1981; Liu and Moncrieff, 2001). In the convective boundary layer, most schemes (both ‘local’ and ‘non-local’) treat momentum transport as a diffusive process, in the sense that convective eddies have a net effect of transporting momentum ‘down-gradient’, from heights where the horizontal wind is higher to heights where it is lower (Lock *et al.*, 2000). However, in the case of thunderstorms, when convective motions become saturated and acquire a certain degree of organization, observations have suggested that it is not uncommon for the momentum transport to be ‘counter-gradient’, acting in the sense of increasing wind shear.

Clearly the diffusion analogue is inappropriate here, as the implied eddy diffusivity would be negative.

The behaviour of convective momentum flux has been investigated by LeMone *et al.* (1984), who used aircraft data at altitudes up to around 6 km to demonstrate that oceanic squall lines, propagating in a direction normal to the line, tend to exhibit down-gradient momentum transport in the axis of the line, while in the direction of propagation it is often counter-gradient at some levels. LeMone and Moncrieff (1994) showed that this could be explained in terms of the archetypal two-dimensional squall-line model of Moncrieff (1992). Tung and Yanai (2002) found from objective wind-field analyses that momentum transport associated with convection in the westerly-wind phase of the Madden–Julian oscillation is typically counter-gradient, but at later times tends to be down-gradient. Likewise, Zhang and Wu (2003), using two-dimensional cloud-resolving simulations of tropical oceanic convection, found that whether the momentum transport was down- or counter-gradient depends on the wind regime.

Doppler radar can measure the radial velocity of cloud and precipitation with high resolution, in principle providing information on convective motions that one may

\*Correspondence to: Robin J. Hogan, Department of Meteorology, University of Reading, Earley Gate, PO Box 243, Reading RG6 6BB, UK. E-mail: r.j.hogan@reading.ac.uk

use to infer the momentum and mass fluxes associated with convective storms, and hence to evaluate models. A difficulty is that the two tangential components of the wind are not measured directly. The measurements of two or more Doppler radars, together with the continuity equation, can be used to infer the full three-dimensional wind field in a localized region, and indeed this method has been applied to the problem of inferring momentum flux (Lafore *et al.*, 1988; Smull and Houze, 1987). Airborne Doppler radar with conical scan patterns can also be inverted to retrieve the complete wind field (e.g. Jorgensen *et al.*, 1983; Chong and Testud, 1996). In frontal situations, the flow can be assumed to be quasi-two-dimensional, and to estimate vertical motion and momentum flux it is sufficient to apply the continuity equation to the observations of a single radar (Chapman and Browning, 1999).

In this paper, we propose a method for deriving the vertical-wind field and one component of the horizontal-wind field simultaneously, in convective situations, using a single high-resolution Doppler radar. If a sequence of vertical scans, or range-height indicators (RHIs), are obtained in the direction of the mean wind, and the sequence of images is animated, then turbulent structures in the various radar variables can often be tracked by eye from one scan to the next, moving both radially and tangentially. The essence of the technique is to automate the process of tracking structures from scan to scan, enabling the tangential component of the velocity field to be estimated simultaneously with the directly-measured radial-velocity field.

The ability to track features from one image to another has a long history, most significantly in operational meteorology, where a sequence of geostationary-satellite images of clouds is used to derive ‘atmospheric-motion vectors’, i.e. the two horizontal components of the wind at the altitude of the clouds (Leese and Novak, 1971). These are now routinely assimilated into weather-forecast models (e.g. Tomassini *et al.*, 1999). With regard to radar, Reinhart and Garvey (1978), Tuttle and Foote (1990) and Tuttle and Gall (1999) have employed the TREC (‘tracking radar echoes by correlation’) method, in which sequences of horizontal scans of the radar reflectivity factor are used to estimate the horizontal wind in precipitation and in situations where clear-air echoes are detectable. The analysis in the present paper differs from TREC in two important respects. First, we apply the method to RHIs rather than horizontal scans; this enables us to estimate the vertical wind, which is of great interest in convective situations. Secondly, we use radial velocity as the field to be tracked, since over short periods it is a better tracer of the air motions than the radar reflectivity factor, which is more a tracer of the rapidly-falling precipitation particles. The analysis is simplified with a sequence of Doppler-radar images; the radial component of the wind is already available, so only the tangential wind needs to be derived by tracking.

We describe the method in Section 2, and the case study, along with the properties of the radar, in Section 3.

We discuss the vertical-wind retrievals in Section 4, the estimates of mass flux in Section 5, and estimates of momentum flux in Section 6. In Section 7 we present a conceptual model to explain how the counter-gradient momentum fluxes could have occurred. In Section 8 we show that, despite the appearance of the storm as a whole, the configuration of updraughts and convergence lines with respect to the direction of cell motion does not fit the usual paradigm of a multi-cell storm.

## 2. Radial-velocity feature-tracking technique

A sequence of radar (or lidar) RHIs can be used to estimate the vertical wind by tracking turbulent structures resolved at the pixel scale, provided that the radar variable used is a good tracer of the air, there is sufficient vertical structure to be tracked from one scan to the next, and the mean motion in the direction perpendicular to the plane of the scans is small (i.e. the radar is scanning close to the plane of the mean horizontal wind). One might consider using the radar reflectivity factor  $Z$  as the variable to be tracked (e.g. Tuttle and Gall, 1999), and animations of  $Z$  in thunderstorms certainly show a strong effect of vertical motion. However,  $Z$  is effectively a tracer of the cloud and precipitation particles, which may be falling at a significant speed with respect to the air. We use the radial velocity  $v_r$  measured by the radar, as this is not directly related to the nature of the targets, and over time-scales of several minutes can be regarded as a good tracer of the wind. Furthermore, in a turbulent environment (such as a thunderstorm observed by radar, or the convective boundary layer observed by lidar), it has abundant vertical structure, at a range of scales, which can be tracked confidently from one scan to the next. Note that this technique would be expected to work even in the case of *quasi-steady* circulations, such as those in supercell thunderstorms. The reason is that such circulations are at scales of 2 km or larger, while the motions tracked by this technique are at scales of around 250 m, where the velocity structure is turbulent. Hence the resulting random turbulent structures will be advected by the motions at a scale of 2 km or larger, enabling this larger-scale motion to be mapped out, whether it is *quasi-steady* or not.

We now explain how the tangential wind  $v_t$  in the plane of the RHIs can be derived from successive scans of  $v_r$ . It is much easier to interpret two scans in terms of the motion of the air in the intervening time if all the points in the first scan have the same temporal separation from the corresponding points in the second scan. As a sequence of RHIs consists of pairs of upward- and downward-moving scans, we therefore use alternate scans, which will be in the same direction, to estimate  $v_t$ . This is illustrated in Figure 1(a); to estimate  $v_t$  at the time of downward scan  $i$ , one would make use of upward scans  $i - 1$  and  $i + 1$ .

Once two such scans have been chosen, each point in scan  $i - 1$  is considered separately. An area centred

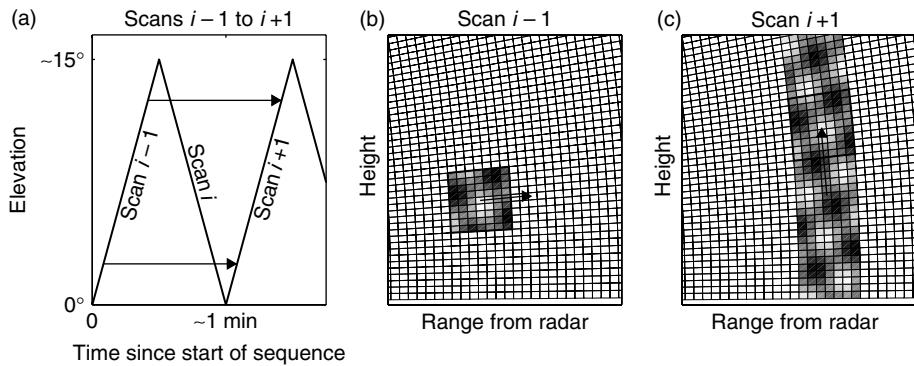


Figure 1. Schematic illustrating the retrieval of tangential velocity from a sequence of radial-velocity scans: (a) elevation versus time for a sequence of vertical scans (RHIs), with the arrows demonstrating that rays at the same elevation in scans  $i-1$  and  $i+1$  are the same time apart; (b) radial velocity in an area of  $7 \times 9$  pixels for scan  $i-1$ , with the arrow indicating how far it would be radially advected (on average) between scans  $i-1$  and  $i+1$ ; (c) the strip of radial velocities in scan  $i+1$  that are compared with the original area in scan  $i-1$ , the vertical arrow indicating the tangential velocity that locates the area with the minimum mean absolute difference from the original area.

on the point under consideration is identified, measuring 7 pixels in range (equivalent to around 2 km for the Chilbolton radar used in this study) and 9 pixels in elevation (equivalent to around  $1^\circ$  for the Chilbolton radar scanning at  $0.5^\circ \text{ s}^{-1}$  with a dwell time of 0.25 s), as shown schematically in Figure 1(b). The values 7 and 9 are chosen simply because they produce the most robust results in the case presented in this paper. The distance that this area would move radially in the time between the two scans is estimated as the measured area-mean radial velocity in the first scan multiplied by the time between the two scans, as illustrated by the arrow in Figure 1(b). If there were no tangential velocity, we could then identify the area of  $7 \times 9$  pixels in the second scan to which the structure in the first scan had been advected (neglecting the small implied divergence or distortion). This area of  $7 \times 9$  pixels in the second scan is then moved tangentially by up to  $n$  pixels in each direction (keeping the radial displacement constant), where  $n$  is chosen to ensure that vertical winds of up to at least  $25 \text{ m s}^{-1}$  can be retrieved. For each pixel displacement, a cost function is calculated: this is defined as the mean absolute difference between the values of  $v_r$  in the areas in the first and second scans. Better results are obtained by weighting the calculation of the mean absolute difference by a Gaussian such that the value at the centre counts for  $e^2$  times more than the values at the corners. The most probable tangential velocity then corresponds to the tangential displacement with the lowest value of the cost function. Figure 1(c) shows the range of data compared with the first scan, with the arrow showing the derived tangential displacement. Note that if any pixels in the area in scan  $i-1$  are missing because no signal was detected, then no tangential wind can be retrieved at that point. Hence it is unfortunately not possible to take the vertical-wind retrieval right up to the edges of the cloud.

The cost function may have multiple minima, and it is generally not the lowest minimum that is the correct one. When multiple minima are detected, the first three minima are compared with the mean of the inferred  $v_t$  from the neighbouring points, and the minimum that

is closest is chosen. Occasionally, there is insufficient vertical structure in the  $v_r$  field within a selected area, in which case it is possible that none of the minima corresponds to the correct  $v_t$ . This problem is largely overcome by a final pass in which each retrieved  $v_t$  pixel is compared to the mean of its neighbours; if the difference exceeds a threshold of  $5 \text{ m s}^{-1}$ , it is deemed to be unreliable and is replaced by the mean of the neighbouring values. It is necessary to then apply a weak smoothing to the retrieved  $v_t$  field. The result is that the effective resolution of the  $v_t$  field is approximately 7 times coarser than the  $v_r$  field from which it is derived. In the case of thunderstorms observed by the Chilbolton radar, the resulting 2 km resolution in range and 1 km resolution in height (at a range of around 50 km) are sufficient to resolve the important vertical convective motions. A scanning boundary-layer lidar applying the same technique would require somewhat higher spatial resolution to derive vertical winds at the important 200–400 m scale.

The final step is to use simple geometry to convert the observed  $v_r$  and derived  $v_t$  into the horizontal and vertical components  $u$  and  $w$  of the wind in the plane of the RHI, accounting for Earth-curvature effects.

### 3. The Gatwick storm

On 28 July 2000, convective storms were widespread over northern France and the whole of the UK. They were forced primarily by surface heating during the day, and as they developed they were slowly advected to the east. This study focuses on a line of cumulonimbus clouds that was observed during the afternoon to the east of the Chilbolton radar in southern England. The national radar network showed the storm to have a distinct line structure for around 2.5 h, from 1530 to 1800 UTC, although it was only studied in detail by the Chilbolton radar between 1600 and 1700 UTC.

Figure 2 shows the 1100 UTC radiosonde ascent from Herstmonceux, around 120 km to the east of Chilbolton,

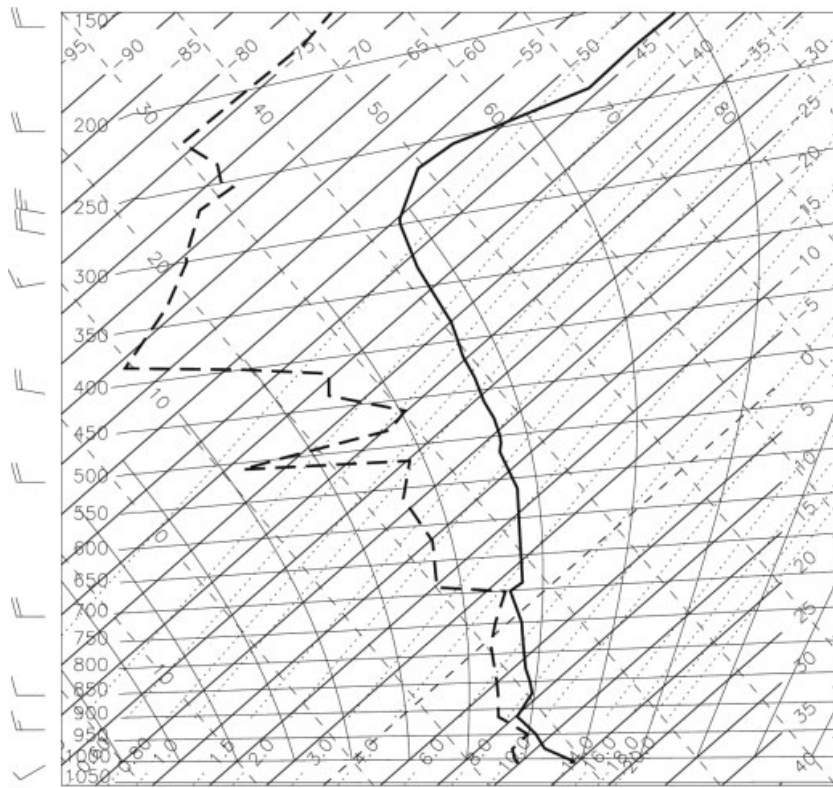


Figure 2. Tephigram of the Herstmonceux radiosonde ascent at 1100 UTC on 28 July 2000. Full wind barbs correspond to winds of 10 knots ( $5.14 \text{ m s}^{-1}$ ).

from which we calculate a convective available potential energy of  $1900 \text{ J kg}^{-1}$  (neglecting virtual temperature and water-loading effects). The wind was from the west, with a speed of  $5\text{--}10 \text{ m s}^{-1}$  at all heights between the boundary-layer top and the tropopause. The cold-point tropopause in Figure 2 is at  $10.0 \text{ km}$  (265 hPa), with a temperature of  $-53^\circ\text{C}$ . The ascent shows a distinct ‘lid’ at  $700 \text{ hPa}$ , a feature that has been found often to be important for modulating the development of deep convection over the UK (Browning *et al.*, 2007; Morcrette *et al.*, 2007).

With its  $25 \text{ m}$  dish, the  $3 \text{ GHz}$  Chilbolton radar (Goddard *et al.*, 1994) is the largest steerable meteorological radar in the world, and has a beam width of only  $0.28^\circ$ . The resulting high vertical resolution, of around  $250 \text{ m}$  at a range of  $50 \text{ km}$ , makes this radar particularly suited to application of the radial-velocity feature-tracking technique. The large dish also gives a high sensitivity, of around  $-25 \text{ dBZ}$  at  $10 \text{ km}$  (for a  $0.25 \text{ s}$  dwell).

Figure 3 shows three low-level plan-position indicators (PPIs) of radar reflectivity factor, around  $20 \text{ min}$  apart. The east–west alignment of the storm is apparent; embedded within it are four distinct cells, labelled A–D, propagating approximately parallel to the orientation of the line at around  $7.5 \text{ m s}^{-1}$ . The lack of discernable propagation of the line in a direction parallel to its axis implies that the storm is not a squall line. It can be seen, however, that the axis of the RHI scans (indicated by the dashed lines) is not always perfectly aligned along the axis of the storm, and there is a small propagation (less

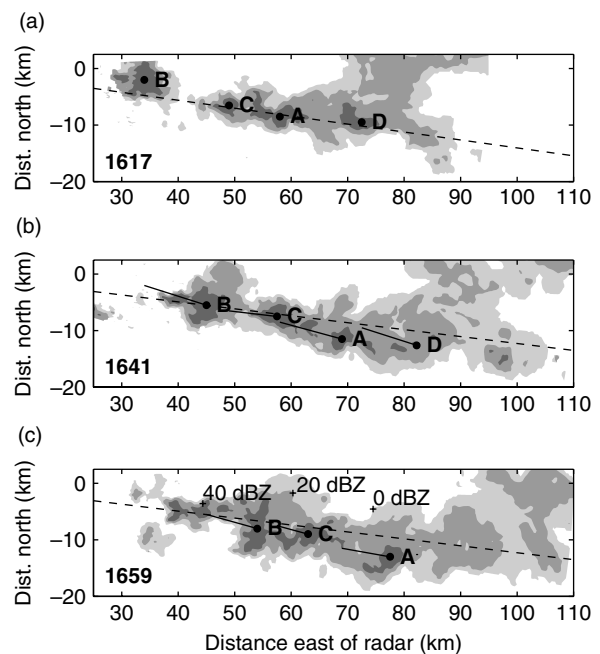


Figure 3. Three low-level horizontal scans of radar reflectivity factor, taken at 1617, 1641 and 1659 UTC, with the three shades indicating values larger than  $0$ ,  $20$  dBZ and  $40$  dBZ, as labelled in panel (c). The centres of the cells A–D discussed in the text are marked by solid circles. In panels (b) and (c), the path of each cell since the previous scan is shown by a black line. Each dashed line indicates the axis of the RHI scan at around the same time. Herstmonceux is slightly outside these images, lying around  $120 \text{ km}$  east and  $25 \text{ km}$  south of Chilbolton.

than  $1 \text{ m s}^{-1}$ ) of individual cells through the plane of the RHIs.

A volume scan of the storm taken by a sequence of PPIs between 1659 and 1705 UTC is depicted in Figure 4, which shows the east–west orientation of the storm (the lowest PPI from this sequence is shown in Figure 3(c)). Within this scan, the three stages of convective development are apparent. At around 40 km to the east of Chilbolton, congestus clouds with tops at around 8 km are visible. Three mature cumulonimbus clouds (cells A–C) lie between 50 km and 80 km from Chilbolton, with cells B and C being associated with a significant anvil cloud. An anvil cloud is apparent beyond 80 km, but the parent cumulonimbus (cell D) has since dissipated.

The highest daily rainfall accumulation by a Met Office MIDAS station in this region was 47 mm, at Old Camp Farm in Lower Beeding, located 81 km east and 12 km south of Chilbolton. Presumably the majority of the rain fell in the hours immediately after the scans shown in Figure 4 were taken, when the line of mature cells passed over the station.

#### 4. Vertical-wind retrievals

Between 1549 and 1652 UTC, the radar performed a sequence of 93 RHIs at azimuths of  $97^\circ$  and  $98^\circ$ , sampling to a range of 110 km. The scan rate was  $0.5^\circ \text{ s}^{-1}$ , and the scans were around 30 s apart. The left-hand column of Figure 5 shows radar reflectivity factors from four of these scans, around 14 min apart, and can be used to track the evolution of the four cells labelled A–D. By also examining the PPIs in Figure 3, we can determine how well the RHIs penetrated the central core of each cell. Cell A had already reached an altitude of 9 km by 1549 UTC, and in Figure 5(a) can be seen to have just penetrated the tropopause at around 10 km. Figure 3(a) shows that even 20 min later it was still well sampled by the RHIs, although the RHIs indicate that it had dissipated by 1630 UTC. Cell B moved into the plane of the RHIs during the course of its evolution, but was well sampled after around 1630 UTC. Cell C was well tracked by the RHIs throughout its evolution from a weakly-precipitating cumulus (Figure 5(d)), through the congestus stage (Figure 5(g)), to penetrating the tropopause (Figure 5(j)). Cell D was the oldest cell and was not well sampled during its active-growth phase.

The corresponding radial Doppler velocity is shown in the central panels of Figure 5, which reveal the very detailed turbulent structure. Regions of horizontal convergence and divergence can be identified. For example, a convergence line is apparent near the surface at a range of 50 km in Figure 5(b), corresponding to the inflow of cell A. On reaching the tropopause, all the cells exhibit strong divergence between 8 km and 10 km.

In animations of the radial velocity, the advection of the turbulent structures by the vertical wind is strongly apparent, particularly in the cores of the storm cells.

The method described in Section 2 has been used to estimate the vertical-wind field for each sequence of three consecutive scans along the same azimuth (so scans  $i - 1$  and  $i + 1$  in Figure 1 would be used to estimate the vertical wind for scan  $i$ ); this is possible for 79 of the original 93 RHIs. The results for four of the scans are shown in the right-hand column of Figure 5.

The strongest updraughts are generally found between altitudes of 5 km and 10 km. Updraughts of up to  $15 \text{ m s}^{-1}$  are found in cell A, while the peak updraughts in cells B–D are around  $10 \text{ m s}^{-1}$ . Naturally no retrievals are possible in cloud-free air, so it is reasonable to assume that the net positive vertical wind that is apparent in the images above 5 km is compensated for by descending motion in the cloud-free areas both within and outside the plane of the scans.

Figure 6 depicts the two-dimensional circulation for the first of the scans in Figure 5 after subtracting the typical cell horizontal propagation velocity of  $7.5 \text{ m s}^{-1}$ . The strong updraught on the westward (trailing) side of cell A can be seen to be fed by westerly flow in the boundary layer, which rises over the slowly-descending easterlies (in a cell-relative sense) in the high-reflectivity region immediately beneath the cell. This configuration of updraughts and downdraughts will be discussed further in Section 7.

Figure 7 shows probability density functions of the horizontal wind  $u$  and the vertical wind  $w$ , as a function of height, for all of the 79 scans for which  $w$  was available. Note that  $u$  has been carefully calculated to be orthogonal to, and at the same resolution as, the  $w$  estimates; the raw radial wind displayed in Figure 5 obviously contains a component of  $w$  at higher elevations. The divergence at cloud top that has been identified in the radial wind is also clearly evident towards the top of Figure 7(a) as a broader spread of  $u$  values. The weak vertical shear of the horizontal wind is responsible for the slight tilt of the some of the cells in Figure 5 (particularly evident in panels (h) and (k)). Figure 7(b) reveals that  $w$  tends to peak at an altitude of around 7.5 km ( $-30^\circ\text{C}$ ). Presumably this is the point at which upward acceleration of positively-buoyant convective elements is balanced by the retarding effect of lateral entrainment.

#### 5. Mass flux

Next we estimate the mass of air carried vertically by a typical convective cell observed in this case. It should be stressed at the outset that this is a very approximate exercise, since only two-dimensional time–height slices were obtained at high frequency, so the size of each cell in the dimension perpendicular to the plane of each scan was not regularly sampled. Nonetheless, reasonable assumptions may be made such that the estimates are accurate to within a factor of around 2. Note that the reported mass flux is specifically for an individual convective cell, and therefore intentionally excludes the compensating downdraughts. Of course, the *net* mass flux including

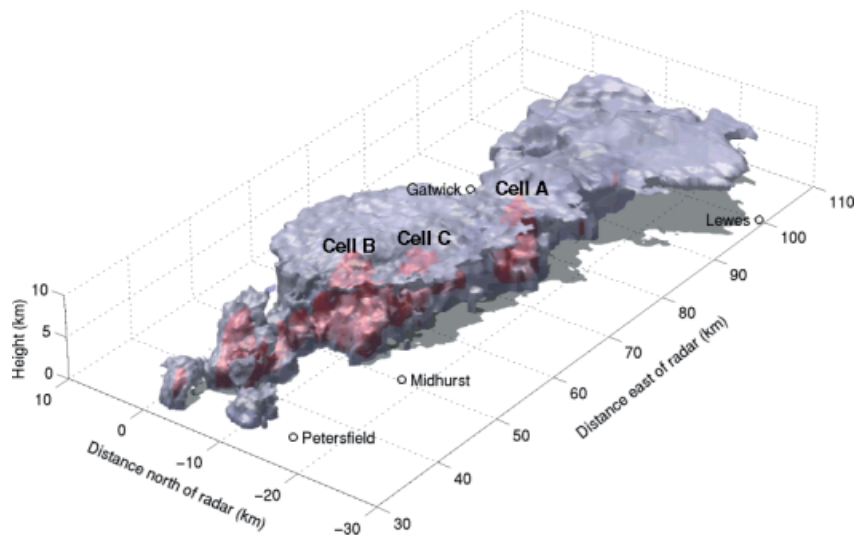


Figure 4. Volume scan through the storm system derived from 12 PPIs,  $0.5^\circ$  apart, between 1659 and 1705 UTC. The 5 dBZ isosurface is shown in grey, and the 30 dBZ isosurface in red.

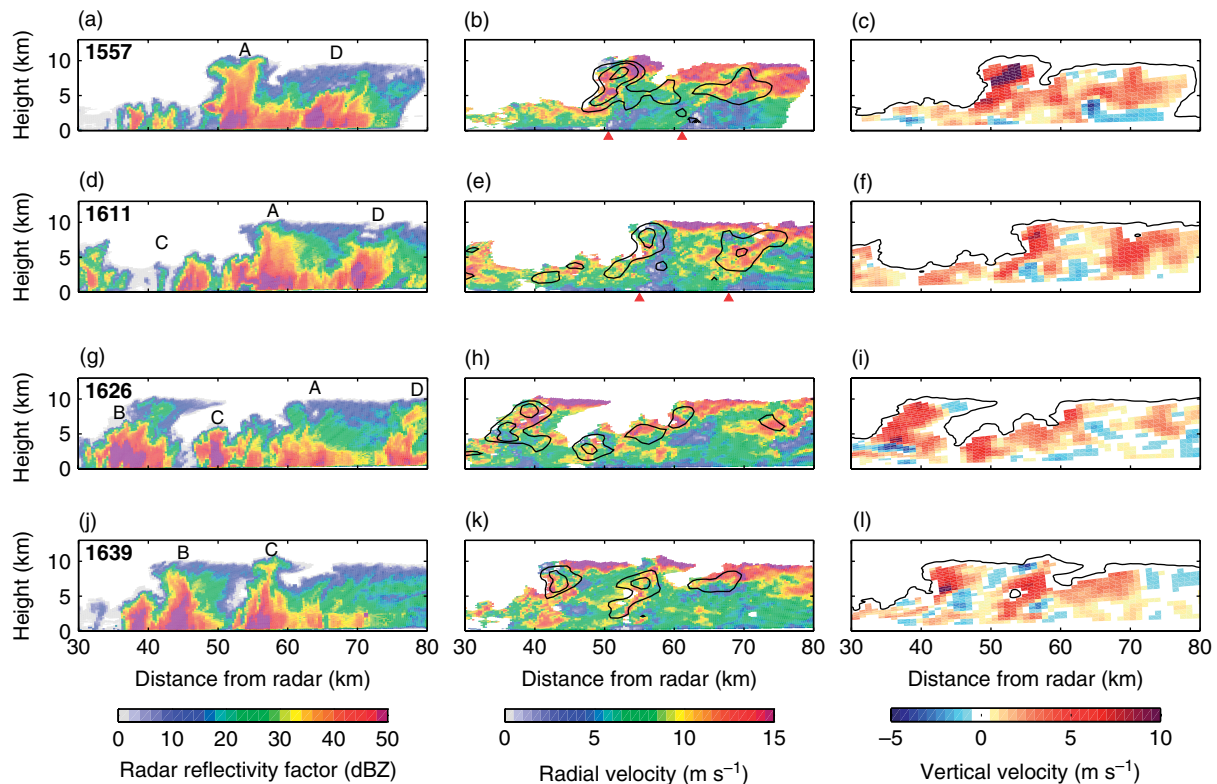


Figure 5. Four RHIs, taken at times of (a, b, c) 1557 UTC, (d, e, f) 1611 UTC, (g, h, i) 1626 UTC and (j, k, l) 1639 UTC (indicated in the leftmost panel of each row): (a, d, g, j) radar reflectivity factor, with the main cells discussed in the text labelled A–D; (b, e, h, k) radial velocity, with black contours indicating vertical winds of  $2 \text{ m s}^{-1}$ ,  $5 \text{ m s}^{-1}$  and  $10 \text{ m s}^{-1}$ ; (c, f, i, l) vertical wind derived using the radial-velocity feature-tracking technique, with the black contour representing the boundary of the detected radar signal. Note that, because of the need to correlate patterns of radial velocity measuring  $7 \times 9$  pixels, the effective resolution of the vertical wind is only around 1–2 km. The red triangles in panels (b) and (e) mark the surface location of convergence lines, discussed in Section 6.

downdraughts over the domain of a numerical-model grid box is essentially the grid-box-mean vertical wind, but what is of interest for convection parametrizations is the mass flux within the convective updraughts (Yanai *et al.*, 1973).

The horizontal location  $x$  of each of the cells A–C (identified in Figure 5) has been tracked by locating

the cell centre by eye in two suitably separated scans, and assuming that the cell is advected horizontally at a constant rate in the intervening time. This analysis has not been performed for cell D, since this cell was already very mature by the start of the scan sequence and so did not exhibit a clearly-defined core. Next, it is assumed that, at a particular height  $z$ , the cell has a circular horizontal

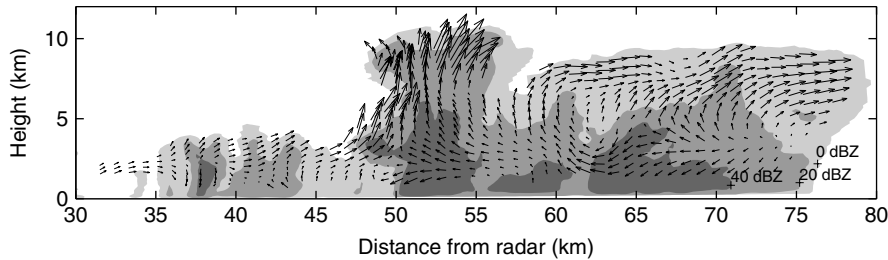


Figure 6. Arrows depicting the two-dimensional cell-relative circulation at 1557 UTC (corresponding to panels (a)–(c) of Figure 5), superimposed on filled contours indicating the radar-reflectivity values. In calculating the cell-relative flow, the cells are assumed to be travelling at  $7.5 \text{ m s}^{-1}$  from left to right (west to east).

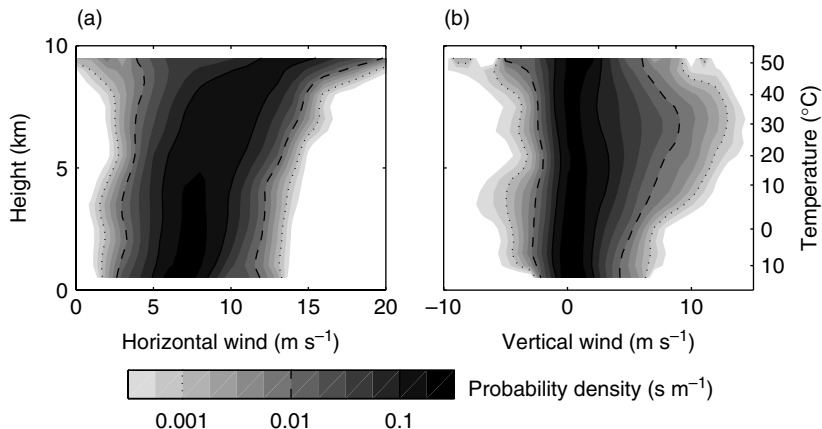


Figure 7. Probability density function at each height of (a) horizontal wind and (b) vertical wind, for the radar observations during the hour-long period discussed in the text. The grey scale is logarithmic.

cross section (confirmed by the nearly-circular reflectivity contours evident in PPI scans at various altitudes) with diameter  $D_c(z)$ , and that each RHI samples through the centre of the cell. The mean vertical wind  $\bar{w}_c(z)$  in the cell is estimated as the mean vertical wind derived from the radial-velocity feature-tracking technique between the ranges of  $x - D_c/2$  and  $x + D_c/2$ . Zipser and LeMone (1980) and May and Rajopadhyaya (1999) have reported that horizontal transects of vertical wind through a convective core tend to have an approximately triangular shape. Thus, if the vertical wind falls to zero at the edge of the cell, then the peak vertical wind at the centre is approximately  $2\bar{w}_c(z)$ . If this triangular shape also occurs in other horizontal directions through the centre of the cell (i.e. if the two-dimensional shape of the vertical wind is ‘conical’), then the instantaneous mass flux at height  $z$  in the cell is given by:

$$M_c(z) = \frac{\pi}{6} D_c(z)^2 \rho \bar{w}_c(z), \quad (1)$$

where  $\rho$  is the density of the air. Clearly the result will be sensitive to the estimated cell diameter. In the case of a cell that has clear air to either side of it at a particular height, the diameter may be taken simply as the width over which a signal was measured. However, most cells are rising through a more extensive region of stratiform cloud and precipitation. In this case, one possible approach would be to use a particular contour

of  $Z$  or  $w$  to define the lateral boundary of the cell. This has several practical difficulties, most notably that the cell is often not sharply distinguished from the surrounding cloud and precipitation at all heights, so that the inferred cell diameter would vary substantially between different heights and from scan to scan.

We therefore take the much simpler approach of assuming a constant cell diameter of  $D_c = 5 \text{ km}$ , but we test the sensitivity of the model to this assumption by also using values of 3 km and 7 km. There are two cases in which the cell diameter is taken to be less than this specified value. First, if some clear-sky air is encompassed by the range  $x \pm D_c/2$  then the diameter is reduced proportionally at that height only. Secondly, in the early stages of cell evolution, if the vertical depth over which a valid signal is recorded is less than  $D_c$  then the inferred diameter of the cell is reduced so that the cell has a one-to-one aspect ratio. Typical cell widths of 5 km are apparent in both the  $Z$  and the  $w$  images in Figure 5; this figure is consistent with the study of May and Rajopadhyaya (1999), who analysed around 60 convective cores using a wind profiler in Darwin, Australia, and reported that the 90th percentile of the diameter distribution was 5 km at an altitude of 5 km.

Panels (a)–(c) of Figure 8 show the resulting instantaneous mass flux as a function of time and height, for the case of  $D_c = 5 \text{ km}$ . The figure also shows the evolution of the heights of the 20 dBZ and 40 dBZ contours.

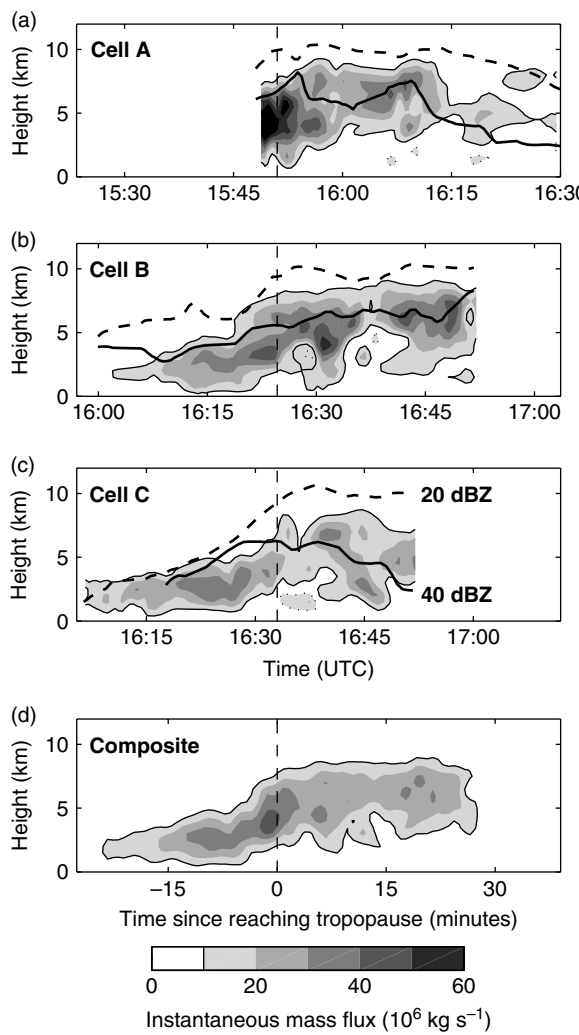


Figure 8. (a, b, c) Estimates of the evolution with time of the mass flux of cells A–C (labelled in Figure 5), calculated as described in Section 5. Positive (upward) fluxes are enclosed by thin solid lines, while negative (downward) fluxes are enclosed by dotted lines. The thick solid and dashed lines indicate the heights of the 20 dBZ and 40 dBZ contours respectively. The temporal axes have been shifted according to the approximate time at which the cell penetrated the tropopause (indicated by the thin dashed vertical line in each plot). (d) Average of cells A–C as a function of the time since reaching the tropopause, excluding periods when only one cell was available.

In the case of cells B and C, the full evolution from cumulus through congestus to mature cumulonimbus is apparent. The long sequence of RHIs only started a short time before cell A reached the tropopause, so its early evolution is unfortunately not captured. There is considerable structure to these figures. While some of it may be attributable to noise in the vertical-wind retrievals and features drifting perpendicular to the plane of the scans, there is support for the contention that the updraughts form in a sequence of ‘bubbles’, as proposed by Yuter and Houze (1995). It is relatively rare for positive mass flux to be present through the entire depth of the troposphere, as is implied by the schematic diagrams of, for example, Browning *et al.* (1976). Additional features to note are the weak downward mass fluxes apparent in the

lower troposphere at various times after the cells penetrate the tropopause; these are likely to have been induced by precipitation immediately below the main updraught region.

To estimate the time-integrated mass flux through the full evolution of a ‘typical’ cell within this storm, we first average the mass flux for the three individual cells, after aligning them according to the approximate times at which they penetrated the tropopause. The result is shown in Figure 8(d). Only periods when two or three cells were available are included in the average. The result spans a period from shortly after the first detection of precipitation (25 min before tropopause penetration) to the time when the cell has largely merged with the region of more extensive stratiform precipitation (around 25 min after tropopause penetration). Even with only three cells averaged, the downdraught regions have disappeared. For a 5 km-wide cell, the typical instantaneous mass flux in Figure 8(d) of around  $3 \times 10^7 \text{ kg s}^{-1}$  corresponds to a mean flux per unit length of  $6000 \text{ kg m}^{-1} \text{s}^{-1}$ . This corresponds to the 90th percentile of the distribution reported by LeMone and Zipser (1980) from aircraft penetrations of the cores of cumulonimbus clouds.

Figure 9 shows the time integral of the instantaneous mass flux depicted in Figure 8(d). The three lines show the calculations for three different values of maximum cell diameter  $D_c$ . Over the typical cell lifetime of 50 min, around 50 megatonnes of air is lofted through the 3 km surface, corresponding to around  $50 \text{ km}^3$  of boundary-layer air. The rapid increase up to 3 km, followed by a near-constant profile to 6 km and then a decrease to 10 km, is consistent with the net effect of the convective cells being to extract air from the lower troposphere and to detrain it at a range of heights above around 6 km.

A figure of 50 megatonnes for a cell of diameter 5 km corresponds to a transport per unit area of  $2500 \text{ kg m}^{-2}$ . From wind-profiler data, May and Rajopadhyaya (1999) report a mean transport of around  $1700 \text{ kg m}^{-2}$  at an altitude of 5 km, but with values of up to  $4000 \text{ kg m}^{-2}$  in the most active cells. However, these values are not entirely comparable to ours, since the vertically-pointing wind profiler only performed a time integration over the

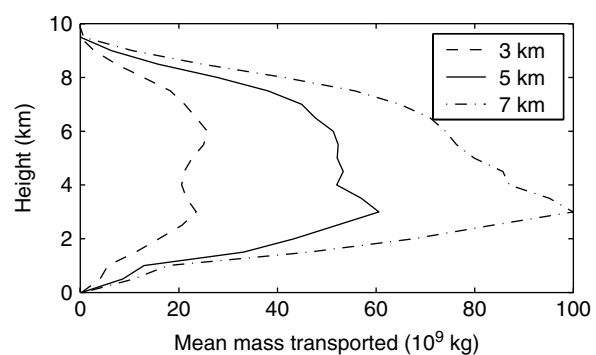


Figure 9. Time-integrated mass transport versus height, for the composite cell shown in Figure 8. The three lines give an approximate indication of the uncertainty, and correspond to three possible values for the maximum cell diameter  $D_c$ , between 3 km and 7 km.

cell as it passed overhead, whereas we are able to track the cells during their full evolution.

## 6. Momentum flux

Having obtained simultaneous estimates of the horizontal wind  $u$  and vertical wind  $w$ , in a direction aligned with the mean horizontal wind, we now attempt to estimate the vertical profile of the total momentum flux  $\bar{uw}$  in this direction over the whole hour-long period. Strictly, this is the flux of momentum-per-unit-mass; the flux of momentum-per-unit-volume would be  $\rho\bar{uw}$  (neglecting correlations of  $\rho$  with wind). By applying Reynolds averaging, in which the instantaneous wind components are split into their mean and fluctuating parts ( $u = \bar{u} + u'$  and  $w = \bar{w} + w'$ ), we may write the total momentum flux as the sum of the contribution  $\bar{uw}$  from the mean wind and the contribution  $\bar{u}'w'$  due to fluctuations from the mean. A complication is that the radar only measures wind components in cloudy or precipitating regions, so it is convenient to further decompose the average momentum flux over a certain horizontal area at a particular height into cloudy (subscript ‘cd’) and clear-sky (subscript ‘cs’) components:

$$\begin{aligned}\bar{uw} &= C\bar{uw}_{\text{cd}} + (1 - C)\bar{uw}_{\text{cs}} \\ &= C\bar{u}_{\text{cd}}\bar{w}_{\text{cd}} + C\bar{u}'\bar{w}'_{\text{cd}} \\ &\quad + (1 - C)\bar{u}_{\text{cs}}\bar{w}_{\text{cs}} + (1 - C)\bar{u}'\bar{w}'_{\text{cs}},\end{aligned}\quad (2)$$

where  $C$  is the fraction of the area that is cloudy (to be discussed later).

The total in-cloud momentum flux  $\bar{uw}_{\text{cd}}$  has been calculated from all 79 scans, and is shown in Figure 10(c). In the interpretation of this plot, it is important to remember that the sample will exclude a significant fraction of the downdraughts, not only those in the clear-sky parts in the plane of the RHIs but also those in the clear-sky air to the north and south of the line of storms. Thus the peak value of  $\bar{uw}_{\text{cd}} = 15 \text{ m}^2 \text{s}^{-2}$  at an altitude of 7 km in Figure 10(c) is largely due to the  $\bar{u}_{\text{cd}}\bar{w}_{\text{cd}}$  term: panels (a) and (b) of Figure 10 show that the mean wind components at this altitude are around  $\bar{u}_{\text{cd}} = 8 \text{ m s}^{-1}$  and  $\bar{w}_{\text{cd}} = 1.9 \text{ m s}^{-1}$ . However, over the grid box of a typical weather-forecast model, compensating downdraughts in clear skies will lead to  $\bar{w}$  being close to zero, and hence  $C\bar{w}_{\text{cd}} \approx -(1 - C)\bar{w}_{\text{cs}}$ . If the values of the clear-sky horizontal winds are similar to the in-cloud values ( $\bar{u}_{\text{cd}} \approx \bar{u}_{\text{cs}}$ ), then there will be a significant cancellation between the mean-wind contributions to momentum flux from the cloudy and clear-sky regions:

$$C\bar{u}_{\text{cd}}\bar{w}_{\text{cd}} \approx -(1 - C)\bar{u}_{\text{cs}}\bar{w}_{\text{cs}}. \quad (3)$$

Figure 10(a) compares the mean horizontal wind from the radar with that from the radiosonde in cloud-free air. It can be seen that the radiosonde profile has much more structure, presumably because it is a single profile through the atmosphere, rather than a temporal and spatial average as in the case of the radar. Nonetheless,

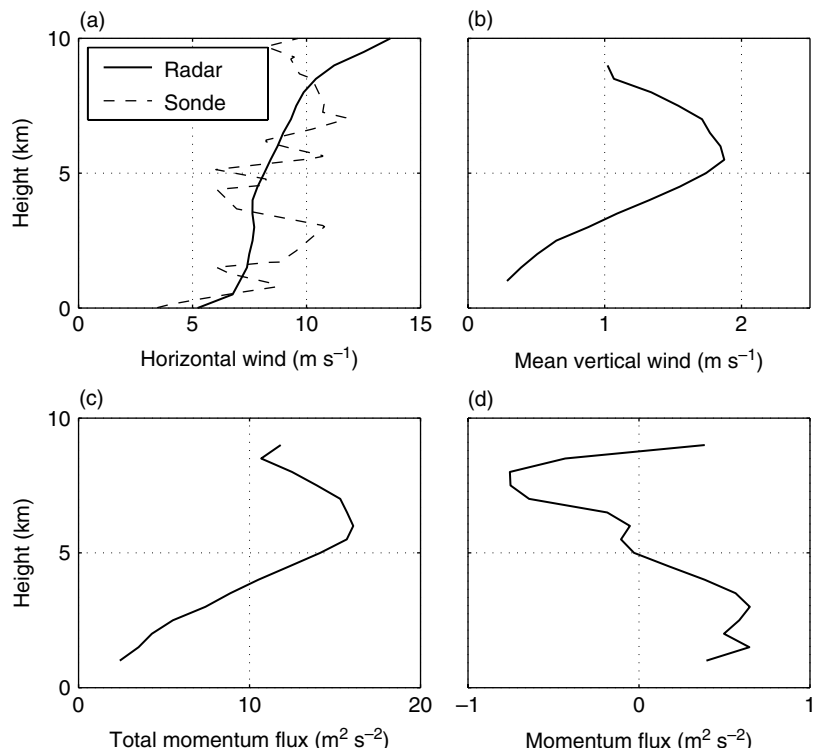


Figure 10. (a) Mean in-cloud horizontal wind  $\bar{u}_{\text{cd}}$  measured by the radar during the hour-long period (79 scans) discussed in the text, together with the component of the wind measured by the radiosonde (Figure 2) in the direction of the radar RHIs. (b) Mean in-cloud vertical wind  $\bar{w}_{\text{cd}}$ . (c) Total in-cloud momentum flux  $\bar{uw}_{\text{cd}}$ . (d) In-cloud momentum flux due to the fluctuating wind  $\bar{u}'\bar{w}'_{\text{cd}}$ . All plots cover the same period.

the root mean square difference between the two is only  $1.5 \text{ m s}^{-1}$ , implying that indeed  $\bar{u}_{cd} \approx \bar{u}_{cs}$ , and therefore a very significant degree of cancellation of total momentum flux is likely. This problem is less significant in the analysis of aircraft observations (LeMone *et al.*, 1984), where both clear-sky and cloudy winds are measured.

It is therefore useful to consider the component of in-cloud momentum flux due to the fluctuating wind,  $\bar{u}'w'_{cd}$ , shown in Figure 10(d). Although this term is much smaller in magnitude than  $\bar{u}_{cd}\bar{w}_{cd}$ , there is no reason to suppose that it is significantly opposed by its clear-sky counterpart. It should be noted at this point that we are assuming that the momentum flux is dominated by motions at or larger than the 1–2 km scale at which the vertical wind is derived. This must be a valid assumption, since if it were not then small-scale motions would make the turbulent patterns impossible to match up between consecutive scans, and the tracking method would not work.

We will now show that if certain assumptions are valid then  $\bar{u}'w'_{cd}$  would be expected to be approximately proportional to the total momentum flux  $\bar{uw}$ . First, if Equation (3) is valid (for example, if the mean vertical wind is zero and the mean cloudy and clear-sky horizontal winds are equal), then two of the terms in Equation (2) can be eliminated. The second assumption is that the clear-sky contribution to the fluctuation momentum flux is zero:  $\bar{u}'w'_{cs} \approx 0$ . This is equivalent to making the reasonable assumptions that in the statically-stable clear-sky air the fluctuations  $u'$  and  $w'$  are of much smaller magnitude than in the cloudy regions, so that even if they are correlated their covariance will be small. (Note that LeMone *et al.* (1984) made an even stronger assumption, that the total momentum flux was dominated by the contribution of the convective cores themselves; this was found to be accurate to within around 25%.) If these assumptions are valid, then Equation (2) reduces to:

$$\bar{uw} \approx C\bar{u}'w'_{cd}. \quad (4)$$

The value of  $C$  depends on how large an area around the storm is considered; it should be large enough to encompass the compensating downdraughts—so at least 20 km to each side of the line of storms—but not large enough to include any of the other storms that occurred on that day.

We now consider the shape of the  $\bar{u}'w'_{cd}$  profile, which Figure 10(d) shows to be positive up to around 4.5 km and negative above this height. Note that outside the height range 1–9 km, the vertical wind is not reliable enough for a robust estimate. The regions of negative momentum flux in areas of positive wind shear can be readily understood as *down-gradient* momentum transport, in the sense that turbulent updraughts ( $w' > 0$ ) will tend to have a lower horizontal wind than the mean ( $u' < 0$ ), and conversely for downdraughts. The large regions of positive momentum flux in the lower troposphere are intriguing, in that the wind shear is still

broadly positive here, so the momentum flux is *counter-gradient*. We can usefully illustrate this by expressing the momentum flux as a diffusive process with eddy diffusivity  $K_m$ :

$$\bar{u}'w' = -K_m \frac{d\bar{u}}{dz}, \quad (5)$$

where  $z$  is height. In the upper troposphere the wind shear is approximately  $d\bar{u}/dz \approx 6 \times 10^{-4} \text{ s}^{-1}$ , and so the momentum flux  $\bar{u}'w'_{cd} \approx -0.6 \text{ m}^2 \text{s}^{-2}$  corresponds to a positive eddy diffusivity of  $K_m \approx 10^3 \text{ m}^2 \text{s}^{-1}$ . However, in the lower troposphere, particularly below 2.5 km where the wind shear is unambiguously positive, the effective eddy diffusivity is negative, at approximately  $-10^3 \text{ m}^2 \text{s}^{-1}$ , so that the paradigm of down-gradient diffusion is invalid. The negative vertical gradient of the momentum flux in the mid-troposphere results in a tendency to accelerate  $\bar{u}$ . In this case the acceleration is around  $-d\bar{u}'w'_{cd}/dz = 3 \times 10^{-4} \text{ m s}^{-2}$ , or  $1 \text{ m s}^{-1} \text{ h}^{-1}$ . Accelerations of the same magnitude were reported by Dudhia and Moncrieff (1987) in a numerical simulation of flow-parallel bands of tropical oceanic convection. Despite the similar morphology, with new cells forming at the trailing end of the line and propagating along it, the sign of their net momentum flux was found to be down-gradient at all altitudes, i.e. it had the effect of smoothing the mean horizontal-wind profile over time. However, their initial wind profile was quite different, having a  $20 \text{ m s}^{-1}$  jet at 600 hPa and much weaker winds above and below it.

Of course, it is possible that the unsampled parts of the flow may be playing a more important role in the overall momentum budget of the storm than is implied by the assumptions made in the derivation of Equation (4). Trier *et al.* (1998) found, in numerical simulations of an arc-shaped propagating squall line, that the momentum flux at the centre of the arc could be explained by two-dimensional conceptual models for linear squall lines, including local counter-gradient momentum flux, but opposing contributions from the different circulations at the edges of the arc meant that the mean momentum flux for the entire system tended to be down-gradient. The morphology of the Gatwick storm is very different from their simulation, with the storm propagation parallel rather than perpendicular to its length, and a linear structure being maintained throughout its evolution. Nonetheless, it would be valuable to validate such an estimate of total momentum flux by its effect on the mean wind profile as observed by radiosondes launched before and after the passage of the storm. Unfortunately, the Herstmonceux ascent 12 h after the one shown in Figure 10(a) also exhibits a rather noisy wind profile, and it is not possible to infer a coherent signal of momentum flux. In any case, individual radiosondes can be unrepresentative of the mean wind profile in convective situations, and in a 12 h period in mid-latitudes the wind profile can evolve significantly because of changes in the large-scale pressure gradient.

## 7. Conceptual model of counter-gradient momentum flux

We now propose a conceptual model to explain how counter-gradient momentum flux could arise in this case. Figure 5(b) shows a sharp change in radial velocity, in the form of convergence lines that reach the ground at 50 km and 61 km from the radar (marked by red triangles). Figures 5(a) and 6 show that the right-hand sides of the convergence regions are associated with very heavy precipitation, while Figure 5(c) shows evidence of descending motion at these locations, presumably induced by a combination of precipitation-drag and cooling due to evaporation. This descending air spreads out to the west and east (left and right respectively in these figures), but the westward-moving part immediately encounters less-dense eastward-moving boundary-layer air at the convergence line, which rises over it and forms the storm inflow.

It is this behaviour that is associated with the counter-gradient momentum flux in the lower troposphere. Figure 11 summarizes in schematic form the slantwise air motions to each side of the convergence line: the descending air ( $w' < 0$ ) to the right of the convergence line is moving westward relative to the mean wind at that altitude ( $u' < 0$ ), while the opposite is true in the ascending region on the left. Hence  $u'w' > 0$ , despite the mean wind shear at that altitude being positive. Moncrieff (1992, figure 10) presented an alternative idealized model to explain how counter-gradient momentum fluxes might occur: the *downshear-tilted eddy*. This is the same as the lower-tropospheric part of Figure 11, but with the slanted updraughts and downdraughts joined at the top

and bottom of the convergence line to form a closed circulation. Note that convergence lines are not so clearly apparent beneath every cell in Figure 5, particularly in the second half of the sequence of scans. This may be due to the sporadic nature of the downdraughts disrupting the low-level inflow from the east.

The air to the left of the convergence line rises to form the main body of the updraught, and carries the lower-tropospheric horizontal momentum with it. This is best illustrated in Figure 5(e), where it can be seen that the core of cell A has a radial velocity throughout its depth of less than  $5 \text{ m s}^{-1}$ . In the upper troposphere, its horizontal velocity is less than the ambient value (so  $u' < 0$ ), and hence  $u'w' < 0$  and the momentum flux is down-gradient. There is some degree of downshear tilt to a number of the updraughts in Figure 5, implying that they experience eastward accelerations as they rise. However, this is less pronounced than the tilt of the circulations near the convergence lines, and so the momentum flux still changes sign in the upper troposphere.

To generalize these points, in a strongly-convective environment there is no reason why momentum flux should be tightly coupled to the local value of the ambient shear, as represented by Equation (5). In the lower troposphere, organized flows lead to the instantaneous horizontal velocities differing so markedly from the environmental mean that the mixing-length concept of upward- and downward-moving eddies tending to carry with them the environmental-mean value of momentum at their original height no longer applies. LeMone *et al.* (1984) argued that in the middle and upper troposphere, the main convective cores are responsible for nearly

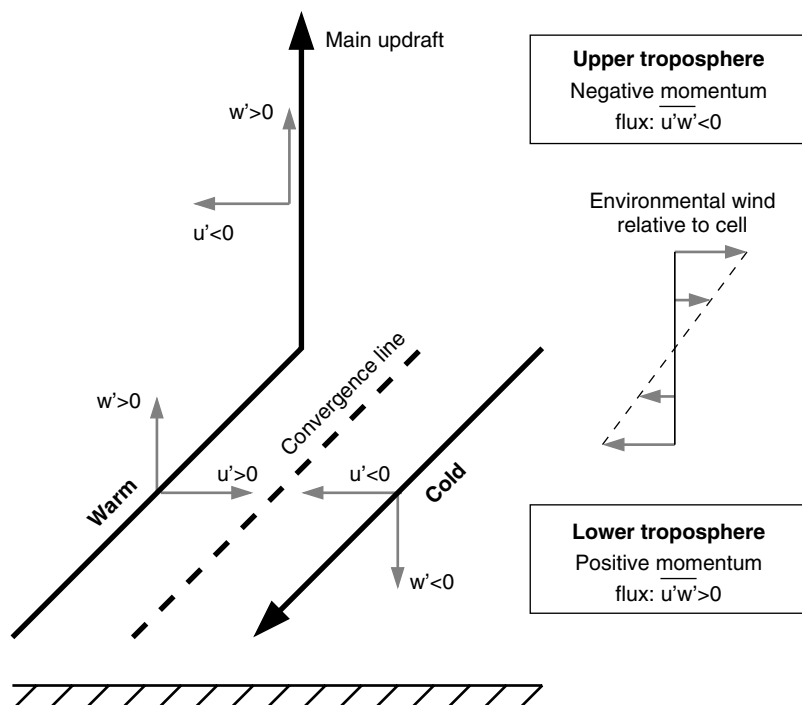


Figure 11. Range–height schematic to explain why momentum flux is positive in the lower troposphere and negative in the upper troposphere. The thick solid arrows depict the main airflows.

all of the momentum transport, and because of their rapid ascent they tend to largely maintain the horizontal momentum they had at their point of initiation, with only weak modification by the environmental wind. Hence one would expect the momentum flux to be down-gradient in the region immediately above the steering level, as in this region the ascending cores would indeed be carrying the environmental-mean momentum, as in mixing-length theory. This is the case above 4.5 km in Figure 10(c). However, should the sign of the environmental wind shear change further up in the troposphere, then the fact that the horizontal momentum in the core is only weakly coupled to the environment would mean that the momentum flux would keep the same sign, and so counter-gradient transport would again be observed. These observations may assist in parametrizing momentum flux in storms of the type observed in this case.

## 8. Classification of the Gatwick storm: multi-cell or line of single cells?

In this section we discuss the morphology of this storm with respect to the classifications previously reported in the literature. The first point to note is that, despite the cells forming in a line (Figures 3 and 4), the storm appears not to have been a squall line, since its propagation speed in the direction perpendicular to the line was only of order  $1 \text{ m s}^{-1}$ . Rather, the cells within the line tended to propagate almost parallel to the line itself. Observations and simulations of such flow-parallel bands are rare in the literature, although Dudhia and Moncrieff (1987) have reported that in the 1974 GATE experiment in the tropical eastern Atlantic, slow-moving or stationary bands were more common than propagating squall lines.

The next question to ask is whether the storm should be classified as a ‘multi-cell’, in the sense that new cells are generated as a consequence of the existing storm (i.e. the storm is self-sustaining), or whether it is simply a line of single cells that are triggered in approximately the same location by a feature of the topography or a mesoscale convergence line. To attempt to answer this question, we have synthesized the main characteristics of the storm in Figure 12(a), with the arrows depicting

the cell-relative flows, derived largely from those shown in Figure 6. An intriguing aspect to this particular storm is that the lower-tropospheric convergence lines, which were seen to play an important role in determining the sign of the momentum flux, move to the east at the same rate as the cell they are associated with, so that the colder air is receding (compare the location of the red arrows in panels (b) and (e) of Figure 5). Hence they have been represented as warm frontal surfaces in Figure 12(a). This is in contrast to almost all conceptual models of multi-cell storms that have been documented before, in which low-level convergence is associated with a gust front that propagates out from a mature cell and initiates new cells. Inspection of the radial wind in low-elevation horizontal scans also shows little evidence for a propagating gust front, at least not to the extent that it is associated with the formation of new cells.

One of the most frequently-cited examples of a non-squall multi-cell storm is the 1973 ‘Raymer hailstorm’, which has been analysed in detail by Chalon *et al.* (1976) and Browning *et al.* (1976), among others. Figure 12(b) depicts the Raymer storm (adapted from the synthesis of Browning *et al.* (1976)). Comparison of panels (a) and (b) of Figure 12 reveals that both storms were composed of a line of cells at various stages of evolution, but there are some crucial differences. First, as mentioned above, the propagating gust front in the Raymer storm appears to play a key role in the maintenance of the storm, by initiating new cells at its leading edge, but such a front is absent from the Gatwick storm. The most important difference is that the propagation direction of the storms are opposite with respect to the major airflows: the Raymer storm features an ‘ascending front-to-rear’ flow, in common with most squall lines and mesoscale convective systems (Newton, 1950; Houze *et al.*, 1989; LeMone and Moncrieff, 1994). The equivalent flow in the Gatwick storm would more accurately be called an ‘ascending rear-to-front’ flow. Likewise, in the Raymer storm the new cells form at the leading end of the sequence, while in the Gatwick storm they tend to form at the trailing end (clearly illustrated in Figure 4). However, this is not always the case. For example, in panels (g) and (j) of Figure 5, cell C can clearly be seen to rise up through the anvil of the older cell B upwind of it.

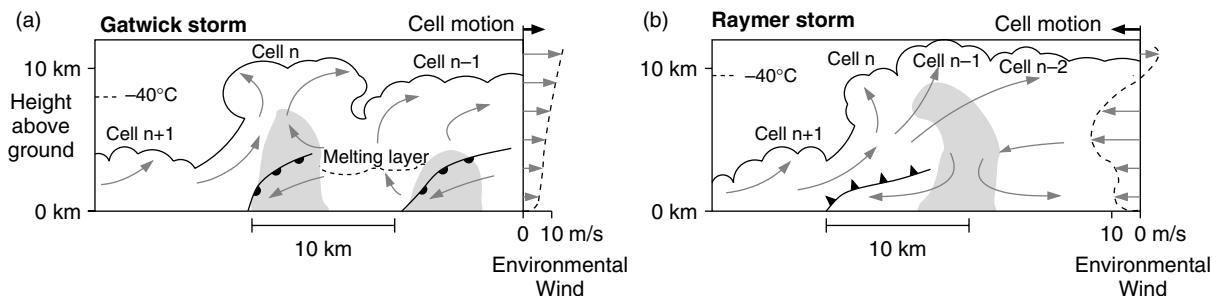


Figure 12. (a) Schematic of the Gatwick storm system, notionally summarizing the 1557 UTC scan shown in panels (a)–(c) of Figure 5 and in Figure 6. (b) Schematic of the Raymer hailstorm, adapted from Browning *et al.* (1976, figure 3) but with the horizontal axis reversed. The arrows show the cell-relative winds, while the shaded region indicates where the radar reflectivity factor exceeded 40 dBZ. In both panels, the cells are labelled in order of their initiation time, with cell  $n + 1$  having formed most recently.

An additional difference is that the cells in the Raymer storm were closer together and tended to merge as they evolved; Chalon *et al.* (1976) report that the new cells propagate to the left (in the coordinate system of Figure 12(b)) at around  $4 \text{ m s}^{-1}$ , but the main body of the storm, including the mature cells, propagates to the left at around  $10 \text{ m s}^{-1}$ . Thus the new cells are absorbed into the main storm complex. This behaviour led Foote and Frank (1983) to propose that the Raymer storm lies somewhere in the continuum between a multi-cell storm (with cells that are clearly separated throughout their evolution) and a supercell (in which a quasi-steady updraught is periodically reinvigorated but remains coherent).

Despite the apparent non-squall nature of the Gatwick storm, previous work to classify squall lines (or mesoscale convective systems) is very relevant here. Parker and Johnson (2000) distinguished between ‘trailing stratiform’ (TS), ‘leading stratiform’ (LS) and ‘parallel stratiform’ (PS) types, indicating the location of the stratiform-rain region with respect to the propagation direction of the line. The TS type was found to be the most common, and the line-perpendicular airflow featured an ascending front-to-rear component similar to that shown in Figure 12(b), with new cells formed at the leading edge of the line. The Gatwick storm, however, shares characteristics with each of the other two types. With regard to the location of the stratiform-rain region, Figure 3 shows it to be parallel to and downwind of the main axis of the storm, as in the PS type. In terms of airflow, the Gatwick storm is closer to the LS type, in which new cells form at the trailing edge of the line. This type is sometimes referred to a ‘back-building’ or quasi-stationary storm, and can be associated with heavy floods due to cells repeatedly reforming in the same location (Schumacher and Johnson, 2005). Pettet and Johnson (2003) provide a schematic of the line-perpendicular airflows in an LS storm, which is similar to the line-perpendicular features in Figure 12(a) and includes both an ascending rear-to-front flow and a trailing warm-frontal convergence line. There are differences, however, notably that these circulations are observed in *line-parallel* cross sections in the case of the Gatwick storm, and the convergence lines appear to remain tied to a particular cell, rather than propagating away (in a storm-relative sense) and initiating secondary cells.

Therefore, perhaps a better classification of the Gatwick storm would be as a sequence of single cells that were triggered in approximately the same location by a feature of the topography rather than the presence of another cell, and were subsequently advected downwind. A possible candidate is the North Hampshire Downs, the highest point of which is 286 m above mean sea level and lies 20 km due north of Chilbolton (altitude 80 m). Conversely, a single cell is characterized by very low wind shear, resulting in the precipitation, once it forms, suppressing the updraught and dissipating the storm within 30–60 min after formation. Certainly the wind shear in the lower troposphere was smaller than

that associated with typical multi-cell storms (Weisman and Klemp, 1982). However, the upper-tropospheric wind shear gave the cells sufficient tilt that the peak in precipitation tended to be downwind of the peak updraught. This is revealed in many of the mature cells shown in Figure 5, and allowed continued updraughts up to 20 min after the cells shown in Figure 8 had reached the tropopause.

Given these arguments, it is clear that the neither the multi-cell nor the single-cell paradigm fully describes the nature of the Gatwick storm. It is known that a continuum of storm types exists between the extremes of multi-cell and supercell (e.g. Foote and Frank, 1983), and we would propose that the Gatwick storm lies somewhere in this supposed continuum between a multi-cell storm and a line of single-cell storms.

## 9. Conclusions

We have shown that by performing a sequence of RHI scans in the plane of the mean wind, one may use a high-resolution Doppler radar to estimate the vertical wind velocity by tracking turbulent features in the radial-velocity field from scan to scan. This technique has been applied to a line of mid-latitude cumulonimbus clouds in which vertical winds up to  $10\text{--}15 \text{ m s}^{-1}$  were retrieved. These retrievals are used to estimate the mass flux of each cell as a function of time and height. The total mass transported by a typical cell, integrated over its lifetime of around 50 min, peaks in the low to middle troposphere at a value of around 50 megatonnes, to within a factor of around 2. In principle, such inferences could be used to evaluate the representation of convection in both parametrization schemes and high-resolution simulations. It is worth noting, however, that most convection schemes predict the mass flux integrated over all the cells in a grid box, so they cannot be directly compared. More recent approaches such as that of Craig and Cohen (2006) can provide a distribution of cell sizes, perhaps making evaluation from observations possible.

The observations reveal the phenomenon of counter-gradient momentum flux in the lower troposphere, which we explain by the mechanism depicted in Figure 11, with rain-induced descent tending to occur on the downshear side of the convergence line that forms at the base of the cells, with the updraught of the storm inflow on the upshear side. One could also apply this mechanism in order to understand the momentum flux associated with a propagating gust front. However, the generality of what has been learned from this case is unclear, since the configuration of the flows with respect to the direction of propagation of the storm seems to differ from that most commonly presented in the literature. While the general appearance of the line of storms in this case immediately suggests a multi-cell, close examination of the Doppler measurements reveals that it lacks the usual gust-front mechanism by which one cell initiates another. Conversely, the shear, although small, provides a sufficient tilt to the cells so that the formation of

precipitation does not rapidly 'kill' the updraught, as in a classical upright single-cell storm. The storm is therefore conjectured to lie somewhere between these two paradigms.

It is worth noting that this study was only possible because of the very high resolution of the Chilbolton radar: a standard weather radar, with a resolution of around 1 km rather than 250 m, would not be able to resolve vertical wind features smaller than around 8 km, a scale that is inadequate for probing the detailed structure of thunderstorms. Furthermore, at 3 GHz the attenuation is relatively low through heavy rain, compared to the higher frequencies more often used operationally.

In this study we were fortunate that the storms were propagating along an azimuth from the radar, so that they could be scanned continuously as they evolved. If this were not the case, then motions through the plane of the scans would have dominated the changes from scan to scan, so that vertical motion could not have been inferred. While this certainly limits the applicability of the radial-velocity feature-tracking technique in the case of radar RHI scans, there is considerable potential for applying the method to scanning high-resolution Doppler-lidar observations of the boundary layer (e.g. Grund *et al.*, 2001). In this case, aerosol particles provide a good signal in all directions, and would allow the Doppler lidar to always be pointed in the plane of the mean wind.

## Acknowledgements

We thank Nicolas Gaussiat, Peter Clark, Phil Krider, Stephen Belcher and Keith Browning for useful discussions during the course of this work. The thunderstorm observations by the Chilbolton 3 GHz radar were funded by NASA (grant Y701089). The Chilbolton radar is operated and maintained by the Rutherford Appleton Laboratory. The surface rainfall data were provided by the Met Office.

## References

- Browning KA, Fankhauser JC, Chalon J-P, Eccles PJ, Strauch RG, Merrem FH, Musil DJ, May EL, Sand WR. 1976. Structure of an evolving hailstorm. 5: Synthesis and implications for hail growth and hail suppression. *Mon. Weather Rev.* **104**: 603–610.
- Browning KA, Blyth AM, Clark PA, Corsmeier U, Morcrette CJ, Agnew JL, Ballard SP, Bamber D, Barthlott C, Bennett LJ, Beswick KM, Bitter M, Bozier KE, Brooks BJ, Collier CG, Davies F, Deny B, Dixon MA, Feuerle T, Forbes RM, Gaffard C, Gray MD, Hankins R, Hewison TJ, Kalthoff N, Khodayar S, Kohler M, Kottmeier C, Kraut S, Kunz M, Ladd DN, Lean HW, Lenfant J, Li Z, Marsham J, McGregor J, Mobbs SD, Nicol J, Norton E, Parker DJ, Perry F, Ramatschi M, Ricketts HMA, Roberts NM, Russell A, Schulz H, Slack EC, Vaughan G, Waight J, Wareing DP, Watson RJ, Webb AR, Wieser A. 2007. The Convective Storm Initiation Project. *Bull. Am. Meteorol. Soc.* **88**: 1939–1955.
- Chalon J-P, Fankhauser JC, Eccles PJ. 1976. Structure of an evolving hailstorm. 1: General characteristics and cellular structure. *Mon. Weather Rev.* **104**: 564–575.
- Chapman D, Browning KA. 1999. Release of potential shearing instability in warm frontal zones. *Q. J. R. Meteorol. Soc.* **125**: 2265–2289.
- Chong M, Testud J. 1996. Three-dimensional air circulation in a squall line from airborne dual-beam Doppler radar data: A test of coplane methodology software. *J. Atmos. Oceanic Technol.* **13**: 36–53.
- Craig GC, Cohen BG. 2006. Fluctuations in an equilibrium convective ensemble. 1: Theoretical formulation. *J. Atmos. Sci.* **63**: 1996–2004.
- Dudhia J, Moncrieff MW. 1987. A numerical simulation of quasi-stationary tropical convective bands. *Q. J. R. Meteorol. Soc.* **113**: 929–967.
- Foote GB, Frank HW. 1983. Case study of a hailstorm in Colorado. 3: Airflow from triple-Doppler measurements. *J. Atmos. Sci.* **40**: 686–707.
- Goddard JWF, Eastment JD, Thurair M. 1994. The Chilbolton Advanced Meteorological Radar: a tool for multi-disciplinary atmospheric research. *Electron. Commun. Eng.* **6**: 77–86.
- Grund CJ, Banta RM, George JL, Howell JN, Post MJ, Richter RA, Weickmann AM. 2001. High-resolution Doppler lidar for boundary layer and cloud research. *J. Atmos. Oceanic Technol.* **18**: 376–393.
- Houze RA. 1973. A climatological study of vertical transports by cumulus-scale convection. *J. Atmos. Sci.* **30**: 1112–1123.
- Houze RA, Rutledge SA, Biggerstaff MI, Smull BF. 1989. Interpretation of Doppler weather radar displays of midlatitude mesoscale convective systems. *Bull. Am. Meteorol. Soc.* **70**: 608–619.
- Jorgensen DP, Hildebrand PH, Frush CL. 1983. Feasibility test of an airborne pulse-Doppler meteorological radar. *J. Appl. Meteorol.* **22**: 744–757.
- Lafore J-P, Redelsperger J-L, Jaubert G. 1988. Comparison between a three-dimensional simulation and Doppler radar data of a tropical squall line: Transports of mass, momentum, heat, and moisture. *J. Atmos. Sci.* **45**: 3483–3500.
- Leese JA, Novak CS. 1971. An automated technique for obtaining cloud motion from geosynchronous satellite data using cross correlation. *J. Appl. Meteorol.* **10**: 118–132.
- LeMone MA, Moncrieff MW. 1994. Momentum and mass transport by convective bands: comparisons of idealized dynamical models to observations. *J. Atmos. Sci.* **51**: 281–304.
- LeMone MA, Zipser EJ. 1980. Cumulonimbus vertical velocity events in GATE. 1: Diameter, intensity and mass flux. *J. Atmos. Sci.* **37**: 2444–2457.
- LeMone MA, Barnes GM, Zipser EJ. 1984. Momentum flux by lines of cumulonimbus over the tropical oceans. *J. Atmos. Sci.* **41**: 1914–1932.
- Liu C, Moncrieff MW. 2001. Cumulus ensembles in shear: Implications for parameterization. *J. Atmos. Sci.* **58**: 2831–2842.
- Lock AP, Brown AR, Bush MR, Martin GM, Smith RNB. 2000. A new boundary layer mixing scheme. 1: Scheme description and single-column model tests. *Mon. Weather Rev.* **128**: 3187–3199.
- May PT, Rajopadhyaya DK. 1999. Vertical velocity characteristics of deep convection over Darwin, Australia. *Mon. Weather Rev.* **127**: 1056–1071.
- Moncrieff MW. 1981. A theory of organized steady convection and its transport properties. *Q. J. R. Meteorol. Soc.* **107**: 29–50.
- Moncrieff MW. 1992. Organized convective systems: Archetypal dynamical models, mass and momentum flux theory, and parametrization. *Q. J. R. Meteorol. Soc.* **118**: 819–850.
- Morcrette CJ, Lean HW, Browning KA, Nicol JC, Roberts NM, Clark PA, Russell A, Blyth AM. 2007. Combination of mesoscale and synoptic mechanisms for triggering an isolated thunderstorm: Observational case study of CSIP IOP 1. *Mon. Weather Rev.* **135**: 3728–3749.
- Newton CW. 1950. Structure and mechanism of the prefrontal squall line. *J. Meteorol.* **7**: 210–222.
- Parker MD, Johnson RH. 2000. Organizational modes of midlatitude mesoscale convective systems. *Mon. Weather Rev.* **128**: 3413–3436.
- Pettet CR, Johnson RH. 2003. Airflow and precipitation structure of two leading stratiform mesoscale convective systems determined from operational datasets. *Weather and Forecasting* **18**: 685–699.
- Reinhart RE, Garvey ET. 1978. Three-dimensional storm motion detection by conventional weather radar. *Nature* **273**: 287–289.
- Schumacher RS, Johnson RH. 2005. Organization and environmental properties of extreme-rain-producing mesoscale convective systems. *Mon. Weather Rev.* **133**: 961–976.
- Smull BF, Houze RA. 1987. Dual-Doppler radar analysis of a mid-latitude squall line with a trailing region of stratiform rain. *J. Atmos. Sci.* **44**: 2128–2148.
- Tomassini M, Kelly G, Saunders R. 1999. Use and impact of satellite atmospheric motion winds on ECMWF analyses and forecasts. *Mon. Weather Rev.* **127**: 971–986.
- Trier SB, LeMone MA, Skamarock WC. 1998. Effect of three-dimensional structure on the stormwide horizontal accelerations and momentum budget of a simulated squall line. *Mon. Weather Rev.* **126**: 2580–2598.

- Tung W-W, Yanai M. 2002. Convective momentum transport observed during the TOGA COARE IOP. 2: Case studies. *J. Atmos. Sci.* **59**: 2535–2549.
- Tuttle JD, Foote GB. 1990. Determination of the boundary layer air-flow from a single Doppler radar. *J. Atmos. Oceanic Technol.* **7**: 218–232.
- Tuttle JD, Gall R. 1999. A single-radar technique for estimating the winds in tropical cyclones. *Bull. Am. Meteorol. Soc.* **80**: 653–668.
- Weisman ML, Klemp JB. 1982. The dependence of numerically simulated convective storms on vertical wind shear and buoyancy. *Mon. Weather Rev.* **110**: 504–520.
- Yanai M, Ebsen S, Chu J-H. 1973. Determination of bulk properties of tropical cloud clusters from large-scale heat and moisture budgets. *J. Atmos. Sci.* **30**: 611–627.
- Yuter SE, Houze RA. 1995. Three-dimensional kinematic and microphysical evolution of Florida cumulonimbus. 1: Spatial distribution of updrafts, downdrafts, and precipitation. *Mon. Weather Rev.* **123**: 1921–1940.
- Zhang GJ, Wu X. 2003. Convective momentum transport and perturbation pressure field from a cloud-resolving model simulation. *J. Atmos. Sci.* **60**: 1120–1139.
- Zipser EJ, LeMone MA. 1980. Cumulonimbus vertical velocity events in GATE. 2: Synthesis and model core structure. *J. Atmos. Sci.* **37**: 2458–2469.